Biomimetic Rod-Magnet-Hall-Effect Sensing for Low-Power Airflow Detection in Small Drones

Aiden Chee[1], Plinio Zanini[2]

[1] Taipei American School, Taipei, Taiwan
[2] Center of Engineering, Modeling and Applied Social Science, Federal University of ABC (UFABC), Santo André, Brazil

E-mail: aidenchee123@gmail.com

Keywords: biomimetic sensing; Hall-effect sensor; small drones; airflow sensing; passive sensing; computational simulation

Abstract

Small autonomous drones require lightweight, low-power sensing systems that can detect environmental forces without adding significant payload or computational demand. This study investigates a biomimetic rod–magnet–Hall-effect sensing system inspired by insect antennae and mechanosensory hairs. A computational model was developed to simulate how airflow or physical contact deflects a lightweight rotating rod with an attached permanent magnet. As the magnet moves relative to two Hall-effect sensors, the magnetic field and differential sensor voltage change, allowing rod angle and relative wind speed to be estimated through calibration and inverse modeling. The simulation tested relative airflow speeds from 0 to 20 m/s and included sensor noise, body tilt, and propagated wind-speed uncertainty. Results showed that the system produced a smooth and monotonic voltage response to rod deflection, and estimated wind speed closely followed the true wind speed under idealized model conditions. Uncertainty was highest at very low wind speeds, where rod deflection and voltage changes were small, but remained low across most of the tested operating range. These findings support the feasibility of the rod–magnet–Hall-effect concept as a lightweight biomimetic sensing approach for small drones. Future work should focus on physical prototype testing, wind-tunnel validation, drone-mounted trials, and multi-sensor configurations for directional airflow and contact detection.

1. Introduction

Small autonomous drones are increasingly used in environmental monitoring, inspection, and search-and-rescue because they can access areas that are difficult or dangerous for humans to reach (Floreano & Wood, 2015). However, sensing remains a key limitation for small drones. Many existing systems rely on cameras, lidar, or other active sensing methods, which can require significant power, processing, and payload capacity (Ehsan & McDonald-Maier, 2015). These constraints become more important for smaller platforms, where weight, energy use, and sensitivity to subtle environmental changes directly affect performance.

Biomimetic sensing provides one way to address these limitations by drawing inspiration from biological systems. Insects and other arthropods use lightweight sensory structures, such as antennae and hair-like mechanoreceptors, to detect airflow, vibration, body movement, and physical contact (Sane et al., 2007). Similar to these biological systems, biomimetic robotics often aims to improve performance by translating simple biological principles into engineered designs. Previous research has applied biomimetic ideas mainly to flight mechanics, aerodynamics, and navigation (Liu et al., 2016; Tanaka et al., 2022). However, less attention has been given to passive, antenna-like sensing structures that can detect airflow or contact through mechanical deflection.

This study addresses that gap by investigating a lightweight rod–magnet–Hall-effect sensor system for detecting external forces. The system is designed so that airflow or physical contact deflects a rod with an attached magnet. As the magnet changes position relative to a Hall-effect sensor, the measured magnetic field changes, producing a corresponding variation in output voltage. Because the system detects force through passive mechanical movement rather than by emitting signals, it could provide a simpler and lower-power sensing approach for small drones and other autonomous devices.

This investigation evaluates whether the rod–magnet–Hall-effect sensing approach can provide a reliable and useful method for detecting relative wind speed and external forces on small autonomous systems. For drone applications, the ability to sense airflow and contact could support environmental awareness without requiring high-power or computationally intensive sensing hardware. By modeling the relationship among external force, rod deflection, magnetic-field change, and sensor voltage, this study examines whether the system can both detect force-induced movement and estimate relative wind speed from the measured signal. This makes the approach relevant as a potential low-power sensing mechanism for small drones operating in changing or constrained environments.

2. Materials and Methods

2.1. System Overview

A computational simulation was developed in Python to model a biomimetic airflow and contact sensing system inspired by insect antennae. The system was designed as a passive sensing structure in which airflow or physical contact causes a lightweight rod to rotate. A permanent magnet attached to the rod moves relative to Hall-effect sensors, changing the magnetic field measured by the sensors and producing a voltage response. The model was implemented in Python 3 using NumPy for numerical calculations, SciPy interpolation for calibration, and Matplotlib for visualization. The main system components were a rotating rod, a permanent magnet, two Hall-effect sensors, and a differential dual-sensor voltage configuration.

2.2. Mechanical Rod Model

The rotating rod represented the antenna-like mechanical sensing structure. The total rod length was set to 0.10 m, and the magnet was positioned 0.05 m from the pivot. The rod diameter was 0.004 m. The pivot was located at x = 0 m and z = 0.070 m, and the initial rod angle was set to 0°. The rod was modeled as a rigid body rotating around the pivot with an angular spring constant of k = 0.020 N*m/rad, which was selected as a simulation parameter because it produced measurable rod deflection across the tested force range while keeping the rod angle within the model's calibration range. This restoring stiffness determined how much the rod deflected in response to wind or contact forces.

The global rod angle was defined as $\phi = \theta_0 + \theta + \beta$, where θ_0 is the initial mounting angle, θ is the rod deflection relative to the drone body, and β is the drone/body tilt angle.

Airflow force on the rod was calculated using the aerodynamic drag equation:

$$F_{wind} = \frac{1}{2}\rho C_D A_{proj} v^2 \tag{1}$$

where $\boldsymbol{F_{wind}}$ is the airflow force, $\boldsymbol{\rho}$ = 1.225 kg/m³ is air density, $\boldsymbol{C_D}$ = 1.1 is the drag coefficient, $\boldsymbol{A_{proj}}$ is the projected area of the rod, and $\boldsymbol{v}$ is wind velocity. The projected area was calculated as:

$$A_{proj} = dL\cos(\phi) \tag{2}$$

where $d = 0.010\, m$ is the rod diameter, $L = 0.10$ is the total rod length, and θ is the rod angle. Wind torque was calculated by applying the wind force at the midpoint of the rod:

$$M_{wind} = F_{wind}\frac{L}{2} \tag{3}$$

Physical contact was modeled as an external point force applied to the rod. The contact torque was calculated as:

$$M_{contact} = F_{contact}h \tag{4}$$

where $\boldsymbol{F}_{contact}$ is the applied contact force and h is the contact lever arm. The equilibrium rod angle was determined by balancing wind torque and contact torque against the restoring torque of the rod:

$$F_{wind}\frac{L}{2} + F_{contact}h - k_{\theta}\theta - m_{rod}g\frac{L}{2}\sin(\phi) = 0 \tag{5}$$

Because the projected area depends on the rod angle, the model solved the rod angle iteratively, using numerical methods.

2.3. Magnet and Hall-Effect Sensor Model

The permanent magnet was modelled as a cylindrical magnet attached to the rotating rod. A neodymium magnet with a radius of 0.008 m, a thickness of 0.006 m, and a remnant magnetic field strength of $B_r = 1.35$ T was considered. The magnet volume was calculated as:

$$V_m = \pi r^2 t \tag{6}$$

Using the model dimensions, the magnet volume was approximately $1.21 * 10^{-6}$ m^3. The magnetic dipole moment was calculated as:

$$m = \frac{B_r}{\mu_0}V_m \tag{7}$$

where $y_0 = 4 * 10^{-7}$ H/m is the permeability of free space. As the rod rotated, the magnet position changed according to the rod angle. The magnet position was calculated as:

$$x_m = x_p + L_m\sin(\phi)$$

(8)

$$z_m = z_p - L_m \cos(\phi)$$

(9)

Table 1. Geometric and mechanical parameters used in the rotating-rod model.

Parameter	Symbol	Value	Description
Total rod length	L	0.10 m	Length of the rotating rod
Magnet distance from pivot	L_m	0.05 m	Distance from pivot to magnet
Rod diameter	d	0.004 m	Diameter of the rod
Pivot x-position	x_p	0 m	Horizontal pivot location
Pivot z-position	z_p	0.070 m	Vertical pivot location
Initial rod angle	θ_0	0º	Initial angular position of the rod
Angular spring constant	k_θ	0.020 N·m/rad	Rotational stiffness used in the simulation
Initial magnet x-position	x_m	0 m	Calculated from $x_m = x_p + L_m \sin(\theta_0)$
Initial magnet z-position	z_m	0.020 m	Calculated from $z_m = z_p - L_m \sin(\theta_0)$

[a] Table footnote.

where x_m and z_m are the magnet coordinates, x_p and z_p are the pivot coordinates, and $L_m = 0.05$ is the distance from the pivot to the magnet.

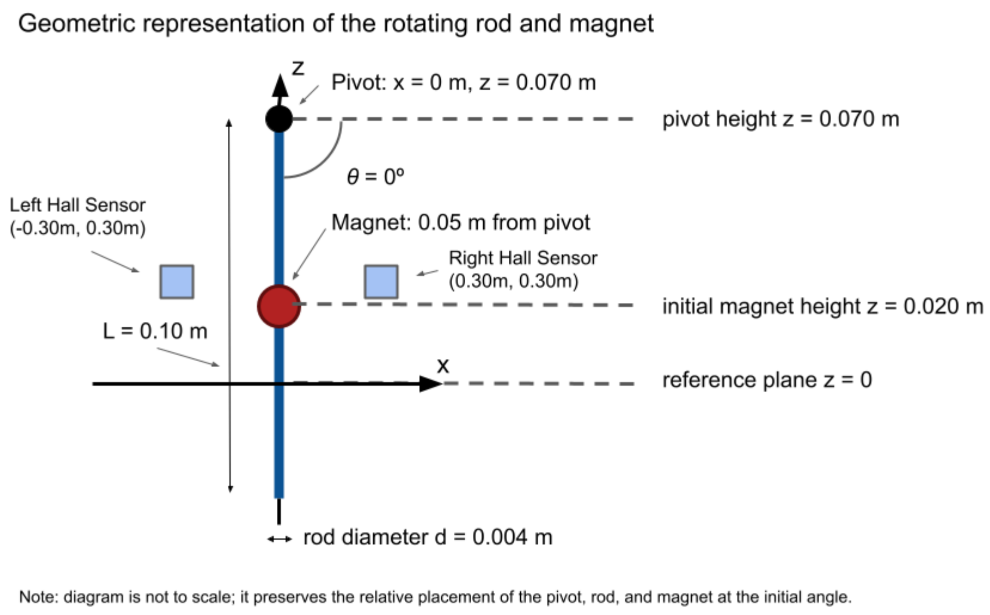

Figure 1. Geometric representation of the rotating rod, pivot, and magnet in the initial position. The pivot is located at x=0 m and z =0.070 m, and the magnet is positioned 0.05 m from the pivot along a 0.10 m rod.

The magnetic field at each Hall sensor was modelled using a magnetic dipole approximation:

$$\vec{B} = \frac{\mu_0}{4\pi r^3}[3(\vec{m} \cdot \vec{\mathrm{r}})\hat{r} - \vec{m}] \tag{10}$$

where $\vec{\boldsymbol{B}}$ is the magnetic field vector at the sensor, $\vec{\boldsymbol{m}}$ is the magnetic dipole moment vector, $\boldsymbol{r}$ is the distance between the magnet and the sensor, and $\hat{\boldsymbol{r}}$ is the unit vector from the magnet to the sensor.

Two Hall-effect sensors were used to measure the magnetic field. The left sensor was positioned at $\boldsymbol{x} = -\mathbf{0.030}$ m and $\boldsymbol{z} = \mathbf{0.030}$ m, while the right sensor was positioned at $\boldsymbol{x} = \mathbf{0.030}$ m and $\boldsymbol{z} = \mathbf{0.030}$ m. The total spacing between the two sensors was therefore $\mathbf{0.060}$ m. At the initial rod position, the magnet was located at approximately $\boldsymbol{x} = \mathbf{0}$ m and $\boldsymbol{z} = \mathbf{0.020}$ m, giving an initial magnet-to-sensor distance of approximately $\mathbf{0.0316}$ m for each sensor. The sensor axis was defined along the x-direction.

The Hall-effect sensor was modelled as a DRV5056-like analog Hall sensor. The simulated sensor used a supply voltage of 5.0 V, a baseline voltage of 0.6 V, a sensitivity of 0.200 V/mT, a full bandwidth of 20,000 Hz, and a magnetic noise density of 130 $\mathrm{T}/\sqrt{\mathrm{Hz}}$. The output voltage was clipped between 0.6 V and 4.9 V. The Hall sensor voltage was calculated as:

$$V_{out} = V_q + SB_{axis} \tag{11}$$

where $\boldsymbol{V_{out}}$ is the output voltage, $\boldsymbol{V_q} = \mathbf{0.6}$ V is the baseline voltage, $\boldsymbol{S} = \mathbf{0.200}$ V/mT is the sensor sensitivity, and $\boldsymbol{B_{axis}}$ is the magnetic field component along the sensor axis.

2.4. Differential Voltage and Noise Model

The left and right sensor voltages were calculated separately. The main sensing signal was the differential voltage:

$$V_{diff} = V_{right} - V_{left} \tag{12}$$

This differential configuration was used to improve sensitivity to magnet displacement. When the rod deflects, the magnet moves closer to one sensor and farther from the other, producing a larger difference between the two voltage outputs.

Electrical noise was simulated using Gaussian random noise. The RMS magnetic noise was calculated as:

$$\sigma_B = B_n\sqrt{f} \tag{13}$$

where $B_n = 130\ \mathrm{T}/\sqrt{\mathrm{Hz}}$ is the magnetic noise density and $f = 50$ Hz is the bandwidth used in the simulation. This produced an RMS magnetic noise of approximately 919 nT. The corresponding single-sensor RMS voltage noise was approximately 0.184 mV. Since the differential signal used two sensors, the differential noise was calculated as:

$$\sigma_{V,diff} = \sqrt{2}\sigma_{V,single} \tag{14}$$

This produced a differential RMS noise of approximately 0.260 mV. The noisy differential voltage was modeled as:

$$V_{diff,noisy} = V_{diff,clean} + N\left(0, \sigma_{V,diff}\right). \tag{15}$$

2.5. Calibration and Wind-Speed Estimation

A calibration function was built to convert differential voltage back into rod angle. The model generated 4,000 rod-angle values from 0° to 45°, calculated the differential voltage for each angle, sorted the voltage-angle relationship, and used interpolation to estimate rod angle from measured voltage. Estimated wind speed was then calculated from the estimated rod angle by rearranging the drag and torque relationship:

$$v = \sqrt{\frac{2\left(k_\theta\theta + m_{rod}g\frac{L}{2}\sin(\phi) - F_{contact}h\right)}{\rho C_D A_{proj}\frac{L}{2}}} \tag{16}$$

2.6. Simulation Conditions

The simulation tested relative airflow speeds from 0 to 20 m/s. This range was selected to span calm to high-flow conditions and to include the upper horizontal flight-speed range of commercially available autonomous drones, such as the Skydio X10, which is manufacturer-rated at 20 m/s maximum horizontal speed, while also covering and exceeding the manufacturer-rated wind-resistance range of common small and professional drone platforms, such as DJI's Mini 4 Pro at 10.7 m/s and Mavic 3M at 12 m/s. A sample test case used a wind speed of 8.0 m/s, a contact force of 0.02 N, a magnet angle offset of 5°, and a noise bandwidth of 50 Hz. For each condition, the model recorded the true wind speed, estimated wind speed, true rod angle, estimated rod angle, left sensor voltage, right sensor voltage, clean differential voltage, and noisy differential voltage.

2.7. Error Propagation

To estimate the uncertainty associated with wind-speed measurements, the model propagated sensor-voltage noise through the calibration and inverse-estimation process. First, the RMS voltage noise of the Hall-effect sensor was calculated from the sensor noise density and measurement bandwidth. The uncertainty in rod angle was then estimated using numerical differentiation of the voltage-to-angle calibration curve:

$$\sigma_\theta = \left|\frac{d\theta}{dV}\right| \sigma_V \tag{17}$$

where σ_θ is the angular uncertainty, V is the voltage uncertainty, and $\frac{d\theta}{dV}$ represents the local sensitivity of the calibration curve.
This follows the general first-order error propagation relationship:

$$\sigma_y = \left|\frac{dy}{dx}\right| \sigma_x \tag{18}$$

where uncertainty in an input variable x produces uncertainty in an output variable y. The derivative can be approximated numerically using a central finite difference:

$$\frac{dy}{dx} \approx \frac{\mathrm{y(x + \Delta x) - y(x - \Delta x)}}{2\Delta \mathrm{x}} \tag{19}$$

In this model, this relationship is applied first to the voltage-to-angle calibration curve. Therefore, Hall-effect sensor voltage noise introduces uncertainty into the estimated rod angle.

The resulting angular uncertainty was then propagated into the wind-speed estimate using finite-difference approximations of the inverse wind-speed model. Uncertainty contributions from both rod-angle estimation and drone-body tilt angle were included:

$$\sigma_\mathrm{v} = \sqrt{\left(\frac{\partial \mathrm{v}}{\partial \theta}\sigma_\theta\right)^2 + \left(\frac{\partial \mathrm{v}}{\partial \beta}\sigma_\beta\right)^2} \tag{20}$$

where σ_v is the uncertainty in estimated wind speed, σ_β is the uncertainty in body tilt angle, and the partial derivatives describe the sensitivity of the wind-speed estimate to changes in rod angle and body orientation. Numerical perturbation methods were used to evaluate these sensitivities.

In this simulation, the main variables that introduce error into the wind-speed estimate are sensor voltage, rod angle, and drone/body tilt angle. Voltage noise affects the estimated rod angle because rod angle is calculated from the voltage-to-angle calibration curve. This angular uncertainty then propagates into the wind-speed estimate because the inverse wind-speed model depends directly on θ. The drone/body tilt angle β also contributes uncertainty because it affects the global rod angle , which changes the projected rod area, gravitational torque, magnet position, and final wind-speed calculation. In a physical drone system, β could be obtained from the drone's onboard IMU, since most drones already use inertial sensors to estimate body orientation. Therefore, including body tilt does not require a fundamentally new sensing system; it adds an existing drone attitude signal into the same error-propagation framework.

This approach allows the model to estimate how electrical noise and orientation uncertainty affect the final wind-speed measurement, providing a first-order assessment of measurement reliability across the tested operating range.

3. Results

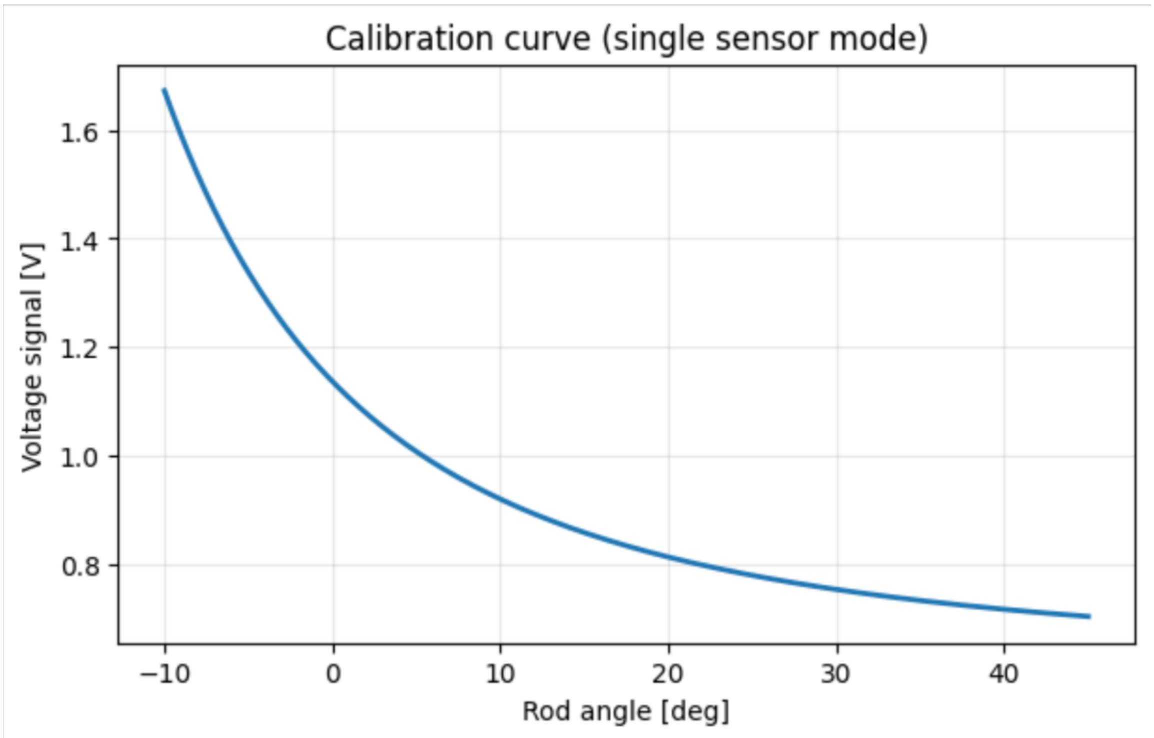

Figure 2. Calibration curve relating rod angle to Hall-effect sensor voltage in single-sensor mode

3.1. Calibration Curve for Single-Sensor Configuration

Figure 2 shows the voltage calibration curve for the single Hall-effect sensor configuration. The calibration curve showed a smooth and monotonic decrease in voltage as the rod angle increased. This result indicates that each rod angle corresponded to a consistent voltage signal in the simulated system. Because the relationship was monotonic, the measured voltage could be used to estimate rod displacement through interpolation.

This result supports the basic sensing principle of the system. As the rod rotated, the attached magnet changed position relative to the Hall-effect sensor, causing the measured magnetic field component to change. The corresponding change in voltage created a usable relationship between mechanical deflection and electrical output. Therefore, the calibration curve demonstrates that the rod–magnet–Hall-effect sensor system can convert rod displacement into a measurable voltage signal.

3.2. Wind Speed to Voltage Signal

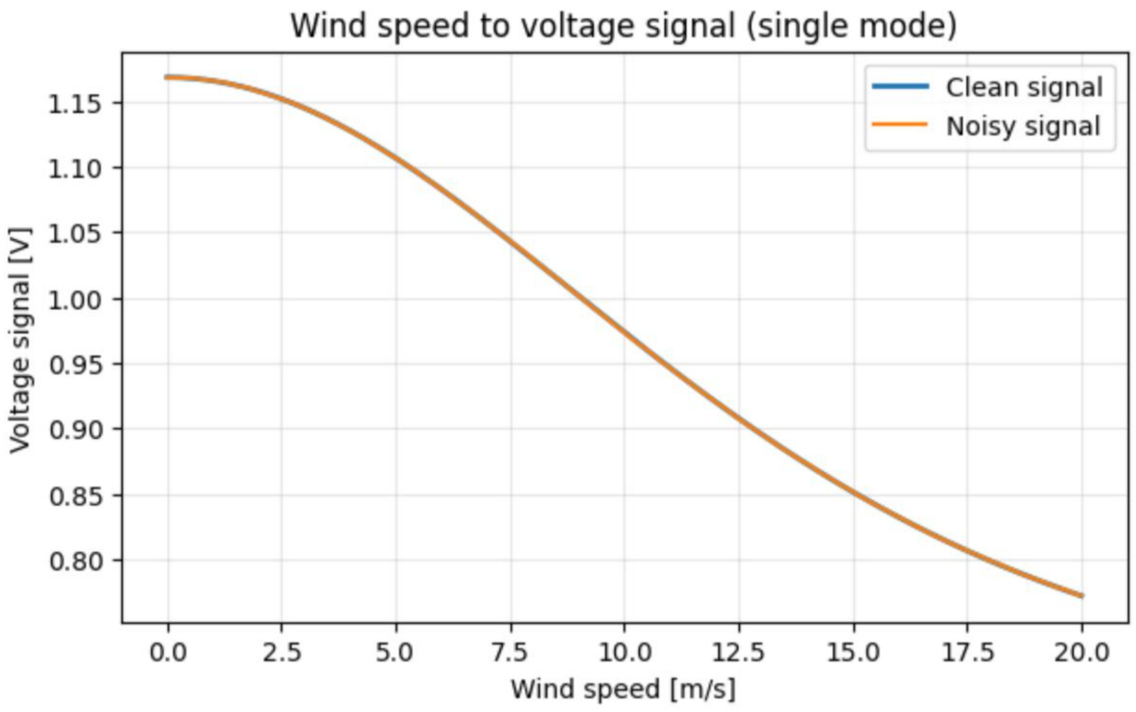

Figure 3. Simulated wind speed to voltage signal response in single-sensor mode

Figure 3 shows the relationship between wind speed and the voltage signal. As wind speed increased, the airflow force on the rod also increased. Stronger airflow caused greater rod deflection, which changed the position of the magnet relative to the Hall-effect sensor. This produced a clear change in the voltage signal across the tested wind-speed range.

The clean and noisy voltage signals nearly overlapped throughout most of the simulation. This indicates that the simulated electrical noise had little effect on the voltage response under the current model assumptions. The small difference between the clean and noisy signals suggests that the modeled Hall-effect sensor noise was low relative to the voltage change caused by rod deflection. As a result, the system showed a stable voltage response to increasing airflow in the simulated environment.

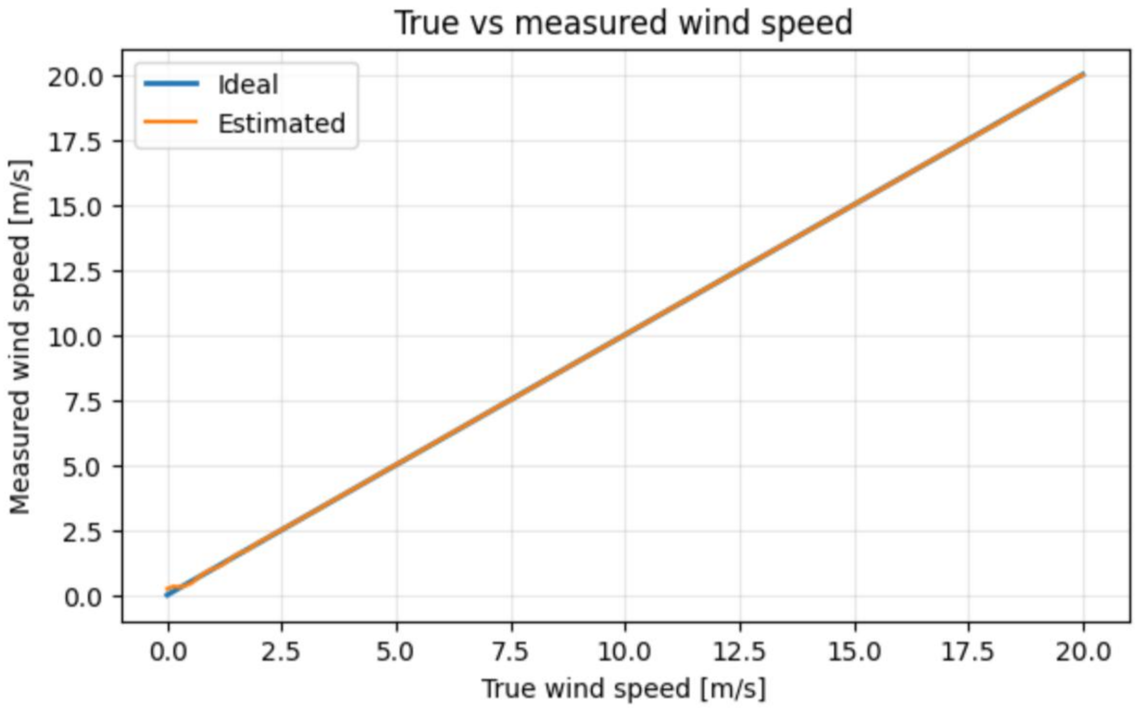

Figure 4. True versus measured wind speed in single-sensor mode

3.3. True versus Measured Wind Speed

Figure 4 compares the true wind speed used in the simulation with the wind speed estimated from the sensor signal. The estimated wind speed closely followed the ideal true-wind-speed line, showing that the forward model and inverse estimation model were internally consistent. In other words, when the simulation generated a rod angle and voltage signal from a given wind speed, the calibration and inverse model were able to reconstruct that wind speed with high accuracy.

This result suggests that the simulated sensing system can estimate wind speed from voltage response under idealized conditions. However, this result does not yet demonstrate real-world accuracy. The model assumes simplified rod mechanics, idealized magnetic dipole behavior, and controlled sensor noise. Physical testing would still be required to determine how accurately the system performs when exposed to real airflow, vibration, drone motion, manufacturing variation, sensor alignment error, and environmental disturbances.

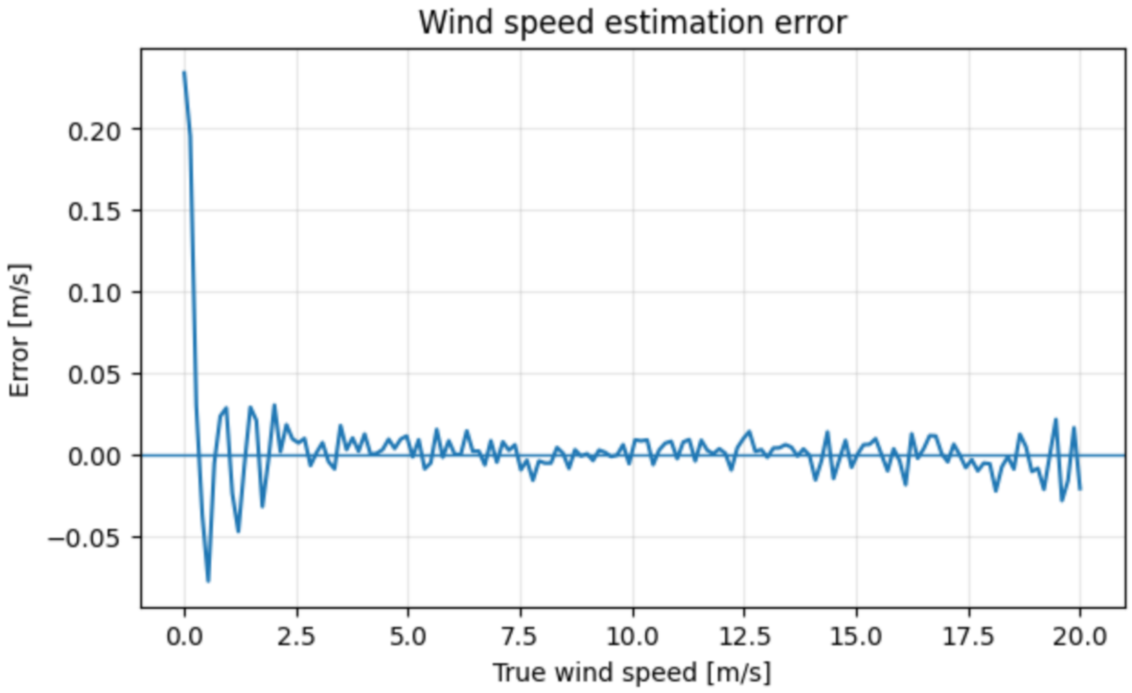

Figure 5. Wind speed estimation error across the simulated airflow range

3.4. Wind Speed Estimation Error

Figure 5 shows the wind speed estimation error, calculated as the difference between estimated wind speed and true wind speed. The estimation error was largest at very low wind speeds. This occurred because low wind speeds produced very small rod deflections. When deflection is small, the resulting voltage change is also small, making the estimate more sensitive to small voltage variations and numerical interpolation error.

Across most of the tested wind-speed range, the estimation error remained close to zero. This supports the internal consistency of the simulation and indicates that the calibration and inverse estimation process worked well over the main operating range. Error increases slightly near the higher end of the tested range. This may be related to changes in voltage sensitivity at larger rod angles, where the relationship between magnet position and Hall sensor voltage becomes less linear.

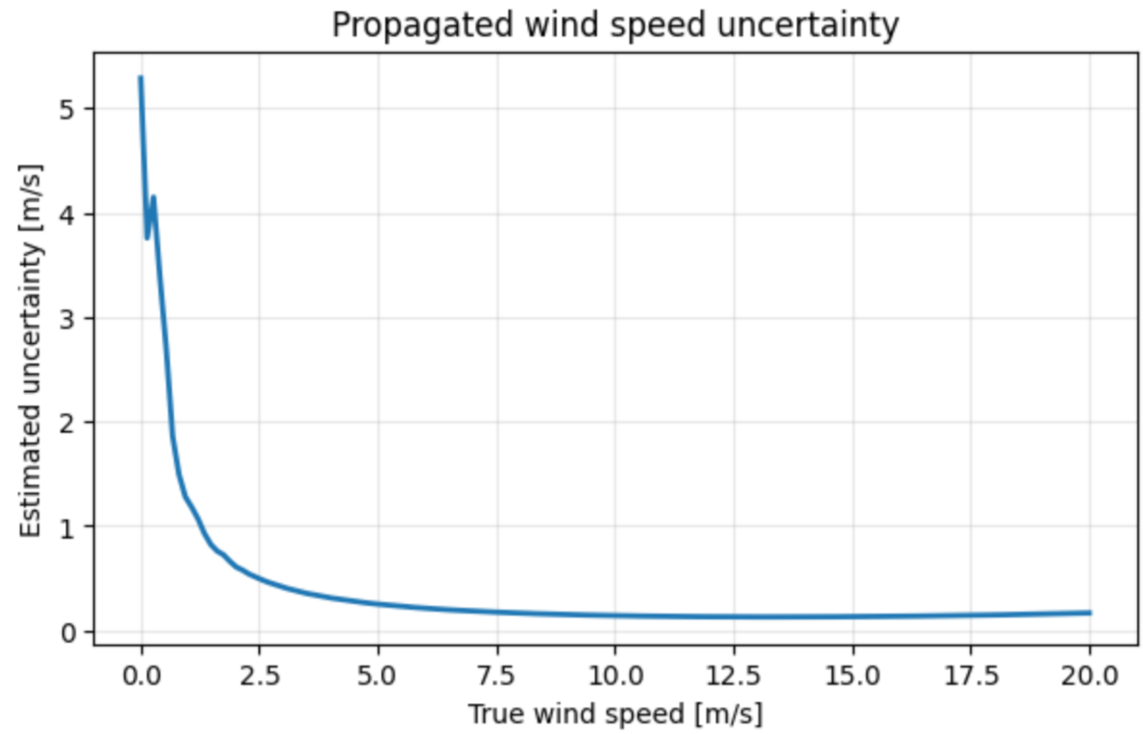

Figure 6. Propagated wind speed uncertainty across the simulated airflow range

3.5. Propagated Wind Speed Uncertainty

Figure 6 shows the propagated uncertainty in the estimated wind speed. The uncertainty was highest near 0 m/s. This is consistent with the wind speed estimation error results, because very low wind speeds generate small rod deflections and small voltage changes. Under these conditions, a small amount of voltage noise can produce a larger relative uncertainty in the estimated angle and wind speed.

Uncertainty decreased quickly as wind speed increased, indicating that the system became more reliable once airflow produced a measurable rod deflection. The system appeared most stable in the middle wind-speed range, where the rod deflection was large enough to create a clear voltage response but not so large that sensitivity began to decrease. At higher wind speeds, uncertainty increased slightly. This trend is consistent with the wind-speed estimation error shown in Figure 4. At very low wind speeds, small rod deflections produce small voltage changes, so a small amount of voltage noise can create a larger relative error in the estimated angle and wind speed. As wind speed increases, the voltage response becomes stronger and the propagated uncertainty decreases. The uncertainty behavior therefore reflects the same angle-to-voltage-to-wind-speed error pathway described by the error-propagation model.

4. Discussion

Overall, the simulation results show that the rod–magnet–Hall-effect sensing system can produce a consistent monotonic voltage response to rod deflection and can reconstruct relative wind speed under ideal model conditions. The strongest performance occurred across the middle of the tested wind-speed range, while the lowest wind speeds were more sensitive to noise and uncertainty. These findings support the feasibility of the sensing concept, but experimental validation is needed to determine whether the same performance can be achieved in a physical drone-mounted system.

The biological motivation for this design originates from the mechanosensory systems of insects. Antennae are not solely olfactory organs; they also function as important mechanosensory structures that provide information about airflow, body orientation, object contact, and flight stability. Sant and Sane (2018) describe insect antennae as multifunctional sensory organs that actively enhance the ability of insects to detect environmental cues through tightly integrated sensory-motor feedback systems. Likewise, mechanosensory hairs found throughout the animal kingdom have evolved to support locomotion, navigation, exploration, and environmental sensing while maintaining high sensitivity and energetic efficiency (Boublil et al., 2021).

The proposed rod–magnet–Hall-effect sensor follows the same functional principle. Environmental forces first produce a mechanical deflection of an external structure, which is then converted into an internal signal. In insects, this conversion is performed by mechanoreceptor neurons located at the base of sensory hairs or antennae. In the present system, the conversion occurs through changes in magnetic field strength measured by Hall-effect sensors. Although the sensing mechanism differs biologically and electronically, both systems rely on passive mechanical displacement as the initial stage of information acquisition.

The comparison is particularly relevant for aerial vehicles because mechanosensory feedback contributes directly to flight control in flying insects. Sane et al. demonstrated that antennal mechanosensory input plays a critical role in flight control in hawkmoths, functioning in a manner analogous to gyroscopic feedback systems. Furthermore, Johnston's organ within insect antennae has been shown to encode antennal position, velocity, direction of movement, airflow, and gravitational stimuli. These findings suggest that insect flight control depends on lightweight mechanical sensors capable of rapidly detecting external disturbances. The proposed rod–magnet–Hall-effect system addresses this idea by using the same basic sensing logic in an engineered form. In the biological system, airflow or contact first causes a lightweight external structure to move, and that movement is converted into a sensory signal. In the proposed design, airflow or contact similarly causes the rod to deflect, while the attached magnet converts that mechanical displacement into a changing magnetic field that can be measured by the Hall-effect sensor. The analogy therefore fits the design because both systems use passive mechanical deflection as the first stage of environmental sensing.

Drone body tilt is another factor that could affect the system because the measured rod deflection depends not only on external airflow or contact, but also on the orientation of the drone body. In the model, this effect is represented by the body tilt angle (β), which is included in the global rod angle (ϕ). As the drone tilts, the rod and magnet position shift relative to the Hall-effect sensor, and the gravitational torque acting on the rod also changes. If this tilt were ignored, part of the voltage change caused by body orientation could be incorrectly interpreted as airflow-induced rod deflection. However, this limitation can be addressed directly because most drones already include IMU measurements of body orientation. By incorporating the IMU-derived tilt angle into the model, the system can account for tilt-related error and propagate its uncertainty through the wind-speed estimate.

The current model represents only a simplified analogue of these biological systems. Real insect antennae contain multiple mechanosensory structures operating simultaneously, including Johnston's organs, Böhm's bristles, hair plates, and other sensilla that provide distributed sensory feedback. By contrast, the present design employs a single sensing element and therefore captures only one aspect of insect mechanosensation.

Future work could investigate arrays of multiple rod sensors positioned around the drone body, potentially providing directional airflow information that more closely resembles the distributed sensing architecture observed in insects. Expanding the system from a single two-dimensional sensing element to a three-dimensional or multi-directional sensing system would be a straightforward extension of the present proof of concept. Multiple rod–magnet–Hall-effect units could be placed at different orientations around the drone body, with each unit using the same relationship between rod deflection, magnet displacement, Hall voltage, and estimated external force. Because each sensing unit operates independently, the expansion to multiple sensors would not require a fundamentally different sensing mechanism. Instead, the system would replicate the same functional unit across several directions to estimate airflow or contact from different parts of the drone body.

5. Conclusion

This study investigated a biomimetic rod–magnet–Hall-effect sensing system inspired by the mechanosensory structures of insects. A computational model was developed to simulate the complete sensing process, including airflow-induced rod deflection, magnetic-field variation, Hall-effect sensor response, calibration, and inverse wind-speed estimation. The results demonstrated that the system produced a smooth and monotonic relationship between rod angle and sensor voltage, allowing mechanical displacement to be reliably converted into an electrical signal and subsequently into an estimate of relative wind speed.

The simulated sensor showed strong internal consistency across the tested operating range. Estimated wind speed closely matched the true wind speed used in the model, while propagated uncertainty remained low throughout most of the range and increased primarily under very low airflow conditions where rod deflections were small. These findings indicate that the sensing concept is capable of translating aerodynamic disturbances into measurable and interpretable signals under idealized conditions.

The model also shows that the system can be extended without major changes to the sensing principle. The inclusion of body tilt angle demonstrates how orientation information from an onboard IMU can be incorporated into the same estimation framework, while the use of multiple rod–magnet–Hall-effect units could expand the design toward three-dimensional or directional sensing. These additions would preserve the basic proof-of-concept mechanism while allowing the system to capture more complex airflow and contact interactions around a drone body.

Beyond its engineering performance, the system demonstrates how biological sensing principles can inspire alternative approaches to environmental awareness in autonomous systems. Similar to insect antennae and mechanosensory hairs, the proposed design relies on passive mechanical interaction with the environment rather than active signal emission. Flying insects use lightweight external sensory structures to detect airflow, orientation changes, and external disturbances while operating under severe size, weight, and energy constraints. The present sensing architecture applies the same functional principle in an engineered form, suggesting a potential pathway toward lightweight and energy-efficient sensing for small aerial robots.

Several limitations remain. The current investigation was entirely computational and relied on simplified assumptions regarding rod mechanics, magnetic-field behavior, and sensor noise. Real-world performance may be affected by factors such as vibration, turbulent airflow, propeller wash, manufacturing tolerances, sensor misalignment, and environmental variability.

Future work should focus on physical prototype testing, controlled wind-tunnel experiments, and drone-mounted flight trials. Additional studies may also explore multi-sensor configurations inspired by the distributed mechanosensory systems found in insects, allowing directional airflow detection and improved environmental awareness. Such developments could help bridge the gap between biological sensing strategies and autonomous robotic platforms.

Overall, the results support the feasibility of the rod–magnet–Hall-effect sensing concept as a lightweight biomimetic sensing mechanism. By combining passive mechanical sensing with simple magnetic-field measurement, the system provides a promising foundation for future research into low-power airflow and contact sensing for small autonomous drones and other mobile robotic systems.

Acknowledgements

The authors thank Indigo Research for providing research mentorship, project guidance, and feedback during the development of this study.

References

[1] B. L. Boublil, C. A. Diebold and C. F. Moss, "Mechanosensory Hairs and Hair-like Structures in the Animal Kingdom: Specializations and Shared Functions Serve to Inspire Technology Applications," Sensors, vol. 21, no. 19, Art. 6375, 2021.
[2] DJI, "DJI Mini 4 Pro Specs." Available: https://www.dji.com/mini-4-pro/specs (accessed Jun. 28, 2026).
[3] DJI Enterprise, "DJI Mavic 3M Specs." Available: https://enterprise.dji.com/mavic-3-m/specs (accessed Jun. 28, 2026).
[4] S. Ehsan and K. D. McDonald-Maier, "On-Board Vision Processing for Small UAVs: Time to Rethink Strategy," in Proc. NASA/ESA Conf. Adaptive Hardware and Systems, 2009, pp. 75–81.
[5] D. Floreano and R. J. Wood, "Science, Technology and the Future of Small Autonomous Drones," Nature, vol. 521, no. 7553, pp. 460–466, 2015.
[6] C. R. Harris et al., "Array Programming with NumPy," Nature, vol. 585, pp. 357–362, 2020.
[7] J. D. Hunter, "Matplotlib: A 2D Graphics Environment," Computing in Science & Engineering, vol. 9, no. 3, pp. 90–95, 2007.
[8] H. Liu, S. Ravi, D. Kolomenskiy and H. Tanaka, "Biomechanics and Biomimetics in Insect-Inspired Flight Systems," Phil. Trans. R. Soc. B, vol. 371, Art. 20150390, 2016.
[9] Python Software Foundation, "Python Language Reference, Version 3." Available: https://www.python.org (accessed Jun. 28, 2026).
[10] S. P. Sane, A. Dieudonné, M. A. Willis and T. L. Daniel, "Antennal Mechanosensors Mediate Flight Control in Moths," Science, vol. 315, no. 5813, pp. 863–866, 2007.
[11] H. H. Sant and S. P. Sane, "The Mechanosensory-Motor Apparatus of Antennae in the Oleander Hawk Moth (Daphnis nerii, Lepidoptera)," J. Comp. Neurol., vol. 526, no. 14, pp. 2215–2230, 2018.
[12] Skydio, "Skydio X10 Technical Specs." Available: https://www.skydio.com/x10/technical-specs (accessed Jun. 28, 2026).
[13] S. Tanaka, A. Asignacion, T. Nakata, S. Suzuki and H. Liu, "Review of Biomimetic Approaches for Drones," Drones, vol. 6, no. 11, Art. 320, 2022.
[14] Texas Instruments, "DRV5056 Ratiometric Unipolar Linear Hall-Effect Sensor." Available: https://www.ti.com/product/DRV5056 (accessed Jun. 28, 2026).
[15] P. Virtanen et al., "SciPy 1.0: Fundamental Algorithms for Scientific Computing in Python," Nature Methods, vol. 17, pp. 261–272, 2020.